

Annihilation of exceptional points from different Dirac valleys in a 2D photonic system

M. Król¹, I. Septembre^{2*}, P. Oliwa¹, M. Kędziora¹, K. Łempicka-Mirek¹, M. Muszyński¹, R. Mazur³, P. Morawiak³, W. Piecek³, P. Kula⁴, W. Bardyszewski⁵, P. G. Lagoudakis^{6,7}, D. D. Solnyshkov^{2,8*}, G. Malpuech^{2*}, B. Piętka^{1*}, J. Szczytko^{1*}

¹*Institute of Experimental Physics, Faculty of Physics, University of Warsaw, Poland*

²*Institut Pascal, PHOTON-N2, Université Clermont Auvergne, CNRS, Clermont INP, Clermont, F-63000 Clermont-Ferrand, France*

³*Institute of Applied Physics, Military University of Technology, Warsaw, Poland*

⁴*Institute of Chemistry, Military University of Technology, Warsaw, Poland*

⁵*Institute of Theoretical Physics, Faculty of Physics, University of Warsaw, Poland*

⁶*Skolkovo Institute of Science and Technology, Bolshoy Boulevard 30, bld. 1, Moscow, 121205, Russia*

⁷*Department of Physics and Astronomy, University of Southampton, Southampton SO17 1BJ, UK*

⁸*Institut Universitaire de France (IUF), F-75231 Paris, France*

Topological physics relies on the existence of Hamiltonian's eigenstate singularities carrying a topological charge, such as quantum vortices, Dirac points, Weyl points and – in non-Hermitian systems – exceptional points (EPs), lines or surfaces¹⁻³. They appear only in pairs connected by a Fermi arc and are related to a Hermitian singularity, such as a Dirac point.

*These authors contributed equally: M. Król, I. Septembre.

The annihilation of 2D Dirac points carrying opposite charges has been experimentally reported ⁴⁻⁶. It remained elusive for Weyl points and second order EPs terminating different Fermi arcs. Here, we observe the annihilation of second order EPs issued from different Dirac points forming distinct valleys. We study a liquid crystal microcavity ⁷ with voltage-controlled birefringence and TE-TM photonic spin-orbit-coupling ⁸. Two neighboring modes can be described by a two-band Hermitian Hamiltonian showing two topological phases with either two same-sign or four opposite-sign Dirac points (valleys). Non-Hermiticity is provided by polarization-dependent losses ^{9,10}, which split Dirac points into pairs of EPs, connected by Fermi arcs. We measure their topological charges and control their displacement in reciprocal space by increasing the non-Hermiticity degree. EPs of opposite charges from different valleys meet and annihilate, connecting in a closed line the different Fermi arcs. This non-Hermitian topological transition occurs only when the Hermitian part of the Hamiltonian is topologically trivial (with four valleys), but is distinct from the Hermitian transition. Our results offer new perspectives of versatile manipulation of EPs, opening the new field of non-Hermitian valley-physics.

The eigenstates of a Hamiltonian combining Hermitian and non-Hermitian parts are, in general, non-orthogonal. Exceptional points (EPs), where the eigenstates coalesce, can appear at the maxima of non-orthogonality when the relative non-Hermiticity is increased. EPs are known in optics for more than a century ¹¹, but only recently they have been shown to allow remarkable phenomena ¹², such as specific lasing ¹³, unidirectional transport ¹⁴, enhanced sensing ¹⁵⁻¹⁸, or scattering control ¹⁹. Their importance has been revealed thanks to their description in terms of a

topological charge, characterizing a topological phase^{1-3,20}, which can be measured by encircling the EP in parameter space^{21,22}. Contrary to 2D Hermitian systems, topological transitions in the non-Hermitian case cannot occur through simple band touching, but only via creation or annihilation of topological charges. So far, the non-Hermitian topological transitions which have been reported were related to the *creation* of EPs^{23,24}. EPs always appear by pair connected by a Fermi arc in the full parameter space, similar to the Weyl points in Hermitian systems, as described by the famous Nielsen-Ninomiya no-go theorem²⁵. Each pair of EPs is formed from a minimum of the Hermitian coupling (e.g. band crossing). In periodic systems, EPs are necessarily located on a closed line in parameter space and an increase of non-Hermiticity leads to the extension of the Fermi arcs which eventually form closed Fermi loops when EPs meet. More complicated situations can occur when more than two oscillators, or two bands get coupled, which leads to the emergence of higher-order singularities^{26,27}.

In this work, we demonstrate a different type of non-Hermitian topological transition in a continuous (non-periodic) 2D photonic system. We show that if the Hermitian Hamiltonian is topologically trivial, the EPs issued from different Hermitian singularities and limiting different Fermi arcs can meet and *annihilate* upon the *increase* of non-Hermiticity.

The system we study is a microcavity filled with a liquid crystal^{7,28} (Fig. 1a). This Fabry-Perot resonator hosts a series of photonic modes with quantized wave vectors perpendicular to the mirror plane and energies E_N (N is the mode number). Each mode forms a polarization doublet showing an in-plane parabolic dispersion with a 2D effective mass which scales as N .

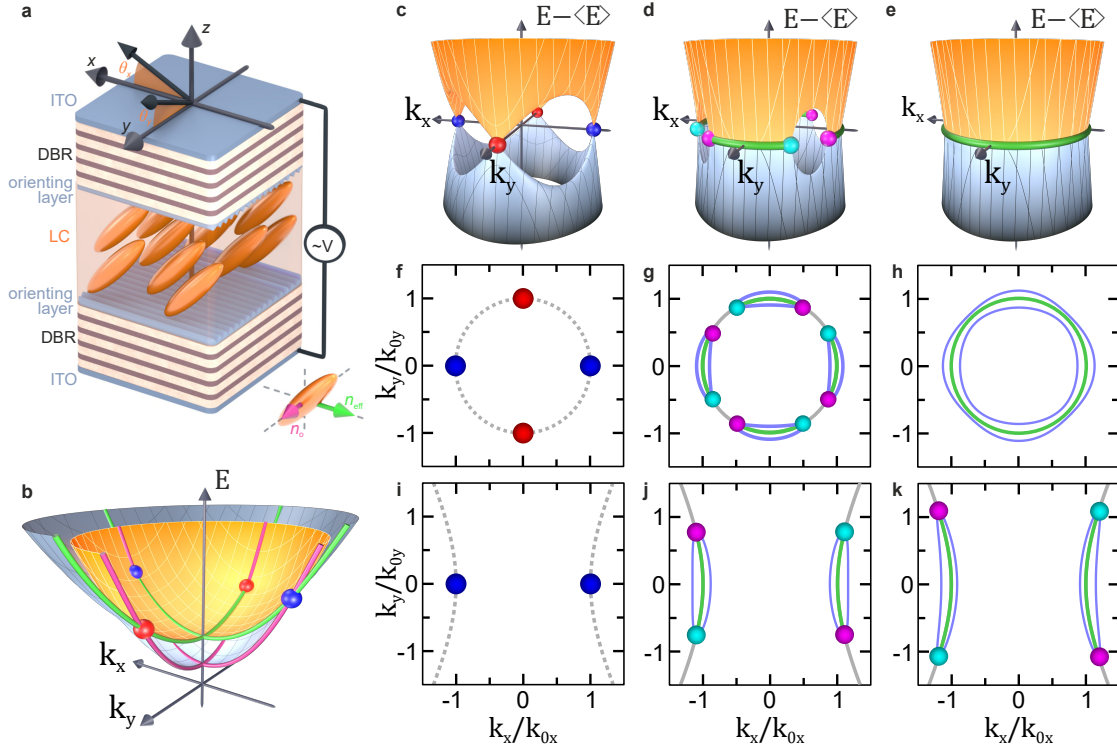


Figure 1: **Scheme of the experiment and the possible behaviors of the exceptional points. a**

Distributed Bragg Reflector (DBR) based microcavity filled by liquid crystal molecules whose orientation is controlled by an external voltage. **b** 2D Energy dispersion of the mode $N + 2$ polarized H at $k = 0$ and of the mode N polarized V at $k = 0$, $k_i = (\omega \sin \theta_i)/c$. **c-e** Difference of the real part of the energies when $\beta' > \beta$ and in the Hermitian case **c**, and non-Hermitian cases for $2\Delta = 3$ meV **d** and $2\Delta = 1.2$ meV **e**. Other used parameters are given in the main text. **f-h** Same as **c-e** but view from the top. The points sets the positions in k -space of the four Dirac points **f** and eight EPs **g**, whereas their colors marks the sign of their topological charges. The dashed line in **f** shows the ellipse given by Eq. (3), setting the allowed positions of EPs. EPs coordinates are determined by the crossing of the ellipse and the blue lines given by $\Omega_r^2 - \Omega_i^2 = 0$. This crossing breaks the ellipse in Fermi arcs shown in green in **g,h** and imaginary Fermi arcs shown in gray in **g**. **i-k** Same as **f-g** but when $\beta' < \beta$ and the Hermitian limits contains only two same sign Dirac points. EPs from different Fermi arcs **j,k** cannot annihilate, belonging to two distinct separated trajectories.

The polarization degeneracy in a doublet is lifted at all wave-vectors except at $k = 0$ (touching parabolas) by the splitting between TE and TM eigenmodes (Transverse-Electric and Transverse-Magnetic). This splitting acts as photonic spin-orbit coupling characterized by a winding number 2^{8,29}. The liquid crystal molecules orientation is set by an external voltage, which controls a tunable linear birefringence α ^{7,28}. A small birefringence $\alpha < (E_{N+1} - E_N)$ lifts the $k = 0$ degeneracy, leading to the formation of two tilted Dirac cones both carrying the same topological Berry charge⁸ $+1/2$. When α becomes comparable with $(E_{N+1} - E_N)$, modes of different parities become energetically close and get coupled by a Rashba-Dresselhaus spin-orbit coupling with equal strength⁷, also called emergent optical activity³⁰. Here we consider $\alpha \approx (E_{N+2} - E_N)$ ²⁸, so that this optical activity is negligible. The corresponding eigenmodes look like two 2D parabola (Fig. 1b). Neglecting the decaying character of modes, these two bands can be described by the following effective 2×2 Hermitian Hamiltonian written on the circular polarization basis:

$$H_{\mathbf{k}}^{real} = \begin{pmatrix} \frac{E_H^{N+2} + E_V^N}{2} + \frac{\hbar^2 k_x^2}{2m_x} + \frac{\hbar^2 k_y^2}{2m_y} & \Delta - \beta' k^2 - \beta(k_x - ik_y)^2 \\ \Delta - \beta' k^2 - \beta(k_x + ik_y)^2 & \frac{E_H^{N+2} + E_V^N}{2} + \frac{\hbar^2 k_x^2}{2m_x} + \frac{\hbar^2 k_y^2}{2m_y} \end{pmatrix} \quad (1)$$

where E_H^{N+2} and $m_H \sim N + 2$ are the energy and mass, of the $N + 2$ th H-polarized mode and E_V^N and $m_V \sim N$, are the energy and mass of the V-polarized mode number N . k_x, k_y are the 2D wave vector components. The spin-independent masses m_x and m_y are determined by the birefringence and the angle of the optical axis (see Supplementary). β is the magnitude of the TE-TM spin orbit coupling. $\beta' = \hbar^2(m_H - m_V)/4m_H m_V$ and $\Delta = (E_H^{N+2} - E_V^N)/2$. This Hermitian Hamiltonian can be written as a linear combination of identity and Pauli matrices, which defines a real effective magnetic field Ω_r acting on the polarization pseudo-spin ($H = \Omega_r \cdot \mathbf{S}$). The two non-zero components of the field are $\Omega_r^x = \Delta - \beta' k^2 - \beta(k_x^2 - k_y^2)$ and $\Omega_r^y = -2\beta k_x k_y$.

This effective Hamiltonian possesses two distinct topological phases described and observed in the Supplementary Materials. If $\beta > \beta'$, the bands show two tilted Dirac cones carrying the same topological charge (Fig. 1i), and the bands are topologically non-trivial, characterized by a non-zero winding of the pseudospin giving rise to a non-zero Chern number, if a gap is opened by breaking the time-reversal symmetry. If $\beta < \beta'$, which is the case in our experiment, the bands possess four tilted Dirac cones, as shown in Fig. 1c,f. Their coordinates are given by $(\pm k_{0x}, 0)$ and $(0, \pm k_{0y})$, where $k_{0,x,y} = (\Delta/(\beta' \pm \beta))^{1/2}$. The winding number of the pseudospin is $+1$ for the two Dirac points located on the k_y -axis, as previously, which corresponds to Berry curvature monopoles of charge $+1/2$. The Dirac points located on the k_x -axis carry a pseudospin winding number -1 and a Berry curvature charge $-1/2$ (Fig. 1f). The corresponding bands are therefore globally topologically trivial, with zero overall pseudospin winding and a vanishing integral of the Berry curvature (Chern number).

The next step is to consider the losses (line broadening), inherently present in photonic systems. Importantly, these losses are significantly different for the H and V modes with $\Gamma_H = 2.04$ meV, $\Gamma_V = 1.8$ meV (see Supplementary Materials). This requires adding an imaginary (non-Hermitian) part to the total Hamiltonian of the system as already illustrated in ⁹:

$$H_{\mathbf{k}} = H_{\mathbf{k}}^{real} + H^{imag} \quad (2)$$

where $H^{imag} = i(\Gamma_0 \mathbb{I}_2 + \delta\Gamma \sigma_x)$ with $\Gamma_0 = (\Gamma_H + \Gamma_V)/2$ is the mean decay rate and $\delta\Gamma = (\Gamma_H - \Gamma_V)/2$ defines a constant imaginary effective field along x : $\Omega_i = (\delta\Gamma, 0, 0)^T$. As shown in Fig. 1d,g, this non-Hermitian part transforms each Dirac point into a pair of EPs ⁹⁻¹¹ connected by a line, called a Fermi arc ³, where the real parts of the eigenvalues are degenerate. The squared

absolute value of the *complex* splitting between the eigenmodes reads $4(|\Omega_r^2 - \Omega_i^2|^2 + 4|\Omega_r \Omega_i|^2)$.

The existence of an exceptional point (zero splitting) therefore requires $\Omega_r \Omega_i = 0$ and $\Omega_r^2 - \Omega_i^2 =$

0. In our case, the first condition reads:

$$\frac{k_x^2}{k_{0x}^2} + \frac{k_y^2}{k_{0y}^2} = 1 \quad (3)$$

which determines an ellipse of possible location for EPs (Fig. 1g, cyan and magenta points). The

second condition $\Omega_r^2 - \Omega_i^2 = 0$ is verified along the blue curves in Fig. 1g,h. The crossing of both

lines sets the coordinates of the 8 EPs which read:

$$k_y^e = \pm \frac{k_{0y}}{\sqrt{2}} \sqrt{1 \pm \sqrt{1 - \delta\Gamma^2/\beta^2 k_{0x}^2 k_{0y}^2}}, \quad (4)$$

$$k_x^e = \pm \frac{k_{0x}}{\sqrt{2}} \sqrt{1 \pm \sqrt{1 - \delta\Gamma^2/\beta^2 k_{0x}^2 k_{0y}^2}}. \quad (5)$$

The Fermi arc, shown in blue-green, is a part of the ellipse where $\Omega_r^2 - \Omega_i^2 < 0$, whereas the

other part, given by $\Omega_r^2 - \Omega_i^2 > 0$ and shown in gray is the imaginary Fermi arc³ with degenerate

imaginary parts of the modes.

The topological charge of an EP can be defined as the winding number of the complex energy of eigenmodes around the EP^{1,2,20}:

$$w = \frac{1}{2\pi} \oint d\mathbf{k} \cdot \nabla_{\mathbf{k}} \arg E_n(\mathbf{k}). \quad (6)$$

The winding numbers of the eight EPs alternate in sign along the ellipse. Increasing $\delta\Gamma$ or decreasing

Δ increases the degree of non-Hermiticity and moves the exceptional points away from the

spawning points along the ellipse, until they meet each other and annihilate, as shown in Fig. 1h.

Fermi arcs connect to form a closed line of trivial degeneracy. We note that it is not a ring of

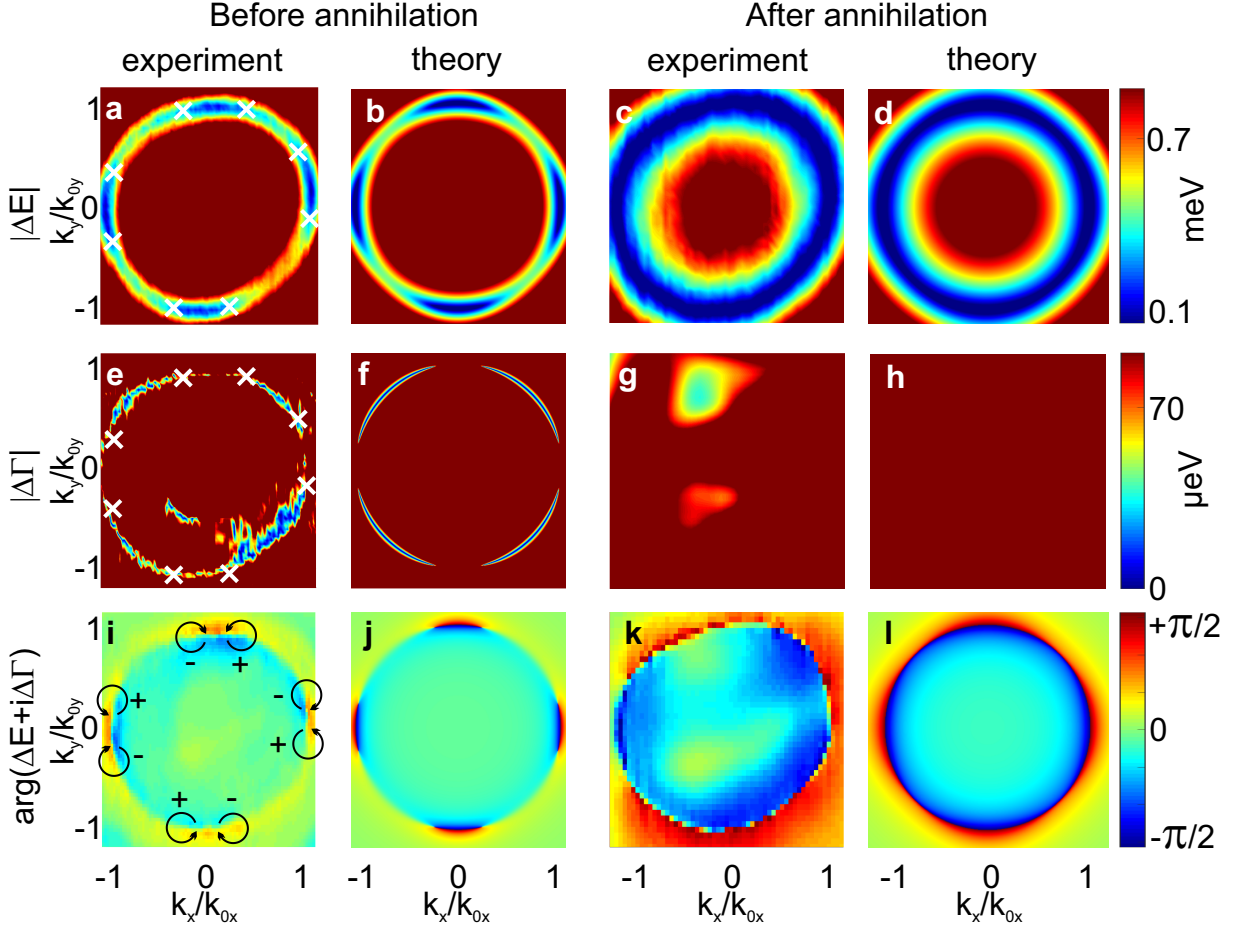


Figure 2: **Observation of EPs, of their topological charges and of their annihilation** Theoretical figures are obtained by diagonalizing the Hamiltonian (2) with parameters given in Methods. The procedure for the extraction experimental energies is detailed in Methods. **a-d** Difference of the real part of the eigenenergies for $2\Delta = 3$ meV (**a,b**) and 1.2 meV (**b,d**). The color bar is saturated above 0.9 meV. The white crosses in **a** shows the EP coordinate limiting the blue area corresponding to Fermi arcs (degenerate real part of energy). **e-h** same as **a-d**, but for imaginary part. The color bar is saturated above 90 μ eV. Imaginary Fermi arcs, where imaginary parts of energies are degenerate, appear in blue. **i,k** Experimental and **j,l** theoretical phase (argument) of the difference of complex energies. EPs are associated to a vortex phase with a phase shift $\pm\pi$ whose winding is shown by the arrows in **i**.

exceptional points reported in ³¹, because the imaginary parts of the energies are not degenerate along this whole line.

As said above, a topological transition occurs for the Hermitian part of the Hamiltonian when $\beta' = \beta$. The system switches between four Dirac points (globally trivial) and two Dirac points (non-trivial, Fig. 1i). This topological transition is demonstrated experimentally in Supplemental Materials. In this case, k_{0y} becomes imaginary. Equation (3) determining the location of EPs remains valid, but describes two hyperbolas, as shown in Fig. 1j,k. EPs issued from distinct Dirac points are moving towards infinity on separated open curves and cannot meet anymore. In such a case, the non-Hermitian topological transition associated with the annihilation of the exceptional points cannot occur. This situation is impossible in periodic systems, where the Fermi lines are necessarily always closed because the periodic energy dispersion is necessarily finite. In continuous systems, such as optical cavities, this situation is typically realized for weak birefringence ⁸, $E_H^N \approx E_V^N$.

Going back to the case $\beta < \beta'$, the non-Hermitian topological transition associated with EP annihilation occurs in Eqs. (5) when $\delta\Gamma = \beta k_{0x} k_{0y}$, which gives

$$\frac{\delta\Gamma}{\Delta} = \frac{\beta}{\sqrt{\beta'^2 - \beta^2}}. \quad (7)$$

One can see that the degree of non-Hermiticity can be changed either by increasing $\delta\Gamma$ or decreasing Δ . The latter option is used in our experiment: Δ is controlled by the voltage affecting the liquid crystal molecules orientation. The experimental study of the liquid crystal cavity is performed by polarization-resolved reflectance, from which we extract the real and imaginary parts of

the energies of the eigenmodes and also their polarization (see Methods). The difference between the real (imaginary) part of the energies versus k_x, k_y are shown in Fig. 2a,e and Fig. 2c,g for two values of detuning $2\Delta = 3$ meV and 1.2 meV for the cases where the EPs are present and annihilated, respectively. In Fig. 2a,e, one can observe the Fermi arcs, where the real parts of energy are degenerate (within the measurement accuracy) and the imaginary parts split. The EPs are shown by white crosses. On the other hand, imaginary Fermi arcs are the lines where the imaginary parts of energies are degenerate and the real parts split. After the EPs annihilation, only a real Fermi arc remains (Fig. 2c,g). We note that in Ref.²⁸, the very same structure was experimentally studied in the same regime of crossing between the $N + 2$ and N modes. The key difference is that the experiment was performed at higher detuning Δ , so that Fermi arcs were expected to be very small, below the grid size in k-space, and thus the EPs could not be resolved. Figure 2b,d,f,h shows the corresponding theoretical results, obtained using the effective non-Hermitian Hamiltonian (2).

The topological charge measurement is presented in Fig. 2i-l. Panels i,k show a map of the phase of the complex energy of the lower mode for $2\Delta = 3$ meV and $2\Delta = 1.2$ meV, as previously. In both cases, the real Fermi arcs appear as a sharp phase shift. Very clear phase vortices are visible at the EPs positions in Fig. 2i and are absent in Fig. 2k. These features are in excellent agreement with the simulations based on the effective non-Hermitian Hamiltonian (2), shown in Fig. 2j,l. The topological charge of each EP $w = \pm 1/2$ is determined by the direction of the phase vortex winding. These charges are opposite for the EPs originating from different Dirac points, which ultimately allows their annihilation.

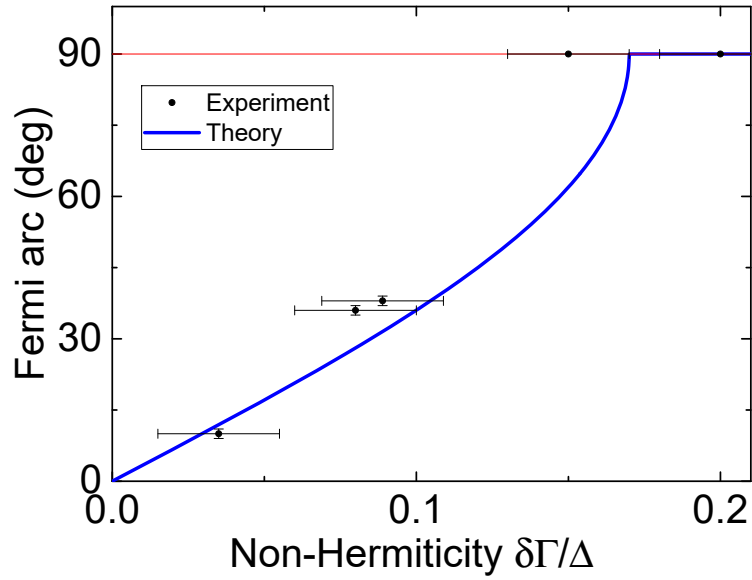


Figure 3: **Moving and annihilating exceptional points.** The length of the Fermi arc as a function of non-Hermiticity. Black points – experiment, blue line – theory. The maximal length of each Fermi arc (90°) is marked with a thin red line. Error bars indicate the measurement uncertainty. The experimental points are obtained by varying the non-Hermiticity degree $\delta\Gamma/\Delta$ by controlling the detuning Δ via applied voltage V .

Figure 3 demonstrates the control of the Fermi arc angular size related to the position of EPs through the experimental tuning of the non-Hermiticity parameter, relate to the detuning. The topological transition associated to the EPs annihilation is clearly visible taking place around $\frac{\delta\Gamma}{\Delta}=0.17$.

Non-Hermitian transitions in two-band systems through EP merging are typically related to a single Hermitian singularity.¹⁻³ Here, we consider the merging of EPs originating from different Dirac points upon *increasing* the non-Hermiticity, which to our knowledge was not reported before, and can be viewed as a first example of non-Hermitian multi-valley physics. Interestingly, the transition we observe could occur only because the Hermitian part of the Hamiltonian is globally topologically trivial. The sum of the topological charges over a band is zero which translates into the presence of a closed line for Fermi arcs. On the contrary, when Hermitian bands are topologically non-trivial, such non-Hermitian topological transition cannot occur. The Hermitian and non-Hermitian transitions allowed by the Hamiltonian representing our system are clearly distinct. On the other side, the possibility to observe the non-Hermitian transition is entirely related to the topology of the Hermitian part. From an applied perspective, our study demonstrate the tuning of the EP coordinates in k-space by simple modification of an external voltage, in a micro-device, at optical frequencies. This ultimately allows to control the angle of emission for the associated chiral modes. Another interest of the planar cavity platform we are using is in that it allows implementing interacting photons modes (exciton-polaritons), up to the blockade regime³². This possibility combined with our present finding could allow to address topological non-Hermitian physics for interacting particles, up to strongly correlated regimes.³²

Methods

Sample The cavity consists of two distributed Bragg reflectors made of 6 $\text{SiO}_2/\text{TiO}_2$ pairs with maximum reflectance at 550 nm grown on glass plates with ITO electrodes. Space between the DBRs is filled with highly birefringent liquid crystal with $\Delta n = 0.41$. To obtain homogeneous orientation of LC both DBRs are finished with structured polymer orienting layer. The total thickness of the LC layer is approx. $1.8 \mu\text{m}$.

Experimental setup Experimental results were obtained in transmission configuration. Broad-band light from a LED diode was focused on the sample with a microscope objective with $50\times$ magnification and numerical aperture $\text{NA} = 0.6$. Transmitted light was collected by another objective with $20\times$ magnification and $\text{NA} = 0.4$. Fourier plane of the collecting objective was imaged on the entrance slit of a monochromator equipped with a CCD camera. Both wave vector directions were measured by scanning of the image across the slit by the automated movement of the imaging lens. Data was collected independently for 6 incident light polarizations; linear: horizontal, vertical, diagonal, antidiagonal and circular σ^+ , σ^- by adjusting angles of half wave plate and quarter wave plate after fixed linear polarizer.

LC layer anisotropy in x - z plane was controlled by external square waveform applied to ITO electrodes with 1 kHz frequency and amplitude of 1.77 V (Fig. 2a,e,i) and 1.72 V (Fig. 2c,g,k).

Linewidth extraction We extract the real and imaginary parts of the energies (that is, the positions and the linewidths) of the modes from the polarization-resolved spectra by fitting them with the Voigt function, in order to account both for the homogeneous broadening due to the mode

lifetime and for the inhomogeneous broadening due to disorder. Only the homogeneous part of the broadening (Lorentzian linewidth) can give rise to non-Hermiticity and is accounted for by the Hamiltonian (2). Parallel computing is used to speed up the extraction for the whole reciprocal space with high resolution. An example of the energy spectrum in two polarizations, together with its fit, is provided in the Supplemental Materials.

Parameters of the Hamiltonian The theoretical panels of Fig. 2 were calculated using the following parameters, obtained from fitting the dispersion and from the linewidth extraction discussed above: $m_x = (1.34 \pm 0.07) \times 10^{-5} m_0$, $m_y = (1.08 \pm 0.06) \times 10^{-5} m_0$, $\beta = 0.080 \pm 0.03 \text{ meV} \mu\text{m}^2$, $\beta' = 0.47 \pm 0.03 \text{ meV} \mu\text{m}^2$. Other parameters were already given in the text, but we provide them here for convenience: $2\Delta = 2.7 \pm 0.1$ and $1.2 \pm 0.1 \text{ meV}$, $2\delta\Gamma = 0.24 \pm 0.05 \text{ meV}$.

1. Leykam, D., Bliokh, K. Y., Huang, C., Chong, Y. D. & Nori, F. Edge Modes, Degeneracies, and Topological Numbers in Non-Hermitian Systems. *Phys. Rev. Lett.* **118**, 040401 (2017). URL <https://link.aps.org/doi/10.1103/PhysRevLett.118.040401>.
2. Shen, H., Zhen, B. & Fu, L. Topological band theory for non-Hermitian Hamiltonians. *Phys. Rev. Lett.* **120**, 146402 (2018). URL <https://link.aps.org/doi/10.1103/PhysRevLett.120.146402>.
3. Bergholtz, E. J., Budich, J. C. & Kunst, F. K. Exceptional topology of non-Hermitian systems. *Reviews of Modern Physics* **93**, 015005 (2021).
4. Tarruell, L., Greif, D., Uehlinger, G., Jotzu, G. & Esslinger, T. Creating, moving and merging

- Dirac points with a Fermi gas in a tunable honeycomb lattice. *Nature* **483**, 302 (2012).
5. Bellec, M., Kuhl, U., Montambaux, G. & Mortessagne, F. Topological transition of Dirac points in a microwave experiment. *Phys. Rev. Lett.* **110**, 033902 (2013). URL <https://link.aps.org/doi/10.1103/PhysRevLett.110.033902>.
 6. Milićević, M. *et al.* Type-III and tilted Dirac cones emerging from flat bands in photonic orbital graphene. *Physical Review X* **9**, 031010 (2019).
 7. Rechcińska, K. *et al.* Engineering spin-orbit synthetic Hamiltonians in liquid-crystal optical cavities. *Science* **366**, 727–730 (2019).
 8. Gianfrate, A. *et al.* Measurement of the quantum geometric tensor and of the anomalous Hall drift. *Nature* **578**, 381–385 (2020).
 9. Richter, S. *et al.* Voigt exceptional points in an anisotropic ZnO-based planar micro-cavity: Square-root topology, polarization vortices, and circularity. *Phys. Rev. Lett.* **123**, 227401 (2019). URL <https://link.aps.org/doi/10.1103/PhysRevLett.123.227401>.
 10. Liao, Q. *et al.* Experimental measurement of the divergent quantum metric of an exceptional point. *Phys. Rev. Lett.* **127**, 107402 (2021). URL <https://link.aps.org/doi/10.1103/PhysRevLett.127.107402>.
 11. Voigt, W. On the behaviour of pleochroitic crystals along directions in the neighbourhood of an optic axis. *Philosophical Magazine Series* **4**, 90 (1902).

12. Miri, M. A. & Alù, A. Exceptional points in optics and photonics. *Science* **363** (2019).
13. Peng, B. *et al.* Loss-induced suppression and revival of lasing. *Science* **346**, 328 (2014).
14. Doppler, J. *et al.* Dynamically encircling an exceptional point for asymmetric mode switching. *Nature* **537**, 76–79 (2016).
15. Hodaei, H. *et al.* Enhanced sensitivity at higher-order exceptional points. *Nature* **548**, 187–191 (2017).
16. Chen, W., Özdemir, Ş. K., Zhao, G., Wiersig, J. & Yang, L. Exceptional points enhance sensing in an optical microcavity. *Nature* **548**, 192–196 (2017).
17. Lai, Y.-H., Lu, Y.-K., Suh, M.-G., Yuan, Z. & Vahala, K. Observation of the exceptional-point-enhanced Sagnac effect. *Nature* **576**, 65–69 (2019).
18. Hokmabadi, M. P., Schumer, A., Christodoulides, D. N. & Khajavikhan, M. Non-Hermitian ring laser gyroscopes with enhanced Sagnac sensitivity. *Nature* **576**, 70–74 (2019).
19. Song, Q., Odeh, M., Zúñiga-Pérez, J., Kanté, B. & Genevet, P. Plasmonic topological metasurface by encircling an exceptional point. *Science* **373**, 1133–1137 (2021).
20. Gong, Z. *et al.* Topological phases of non-Hermitian systems. *Physical Review X* **8**, 031079 (2018).
21. Gao, T. *et al.* Observation of non-hermitian degeneracies in a chaotic exciton-polariton billiard. *Nature* **526**, 554–558 (2015).

22. Su, R. *et al.* Direct measurement of a non-Hermitian topological invariant in a hybrid light-matter system. *Science Advances* **7**, eabj8905 (2021). URL <https://www.science.org/doi/abs/10.1126/sciadv.abj8905>.
23. Zeuner, J. M. *et al.* Observation of a topological transition in the bulk of a non-Hermitian system. *Phys. Rev. Lett.* **115**, 040402 (2015). URL <https://link.aps.org/doi/10.1103/PhysRevLett.115.040402>.
24. Ozturk, F. *et al.* Observation of a non-Hermitian phase transition in an optical quantum gas. *Science* **372**, 88 (2021).
25. Nielsen, H. & Ninomiya, M. A no-go theorem for regularizing chiral fermions. *Physics Letters B* **105**, 219–223 (1981). URL <https://www.sciencedirect.com/science/article/pii/0370269381910261>.
26. Ding, K., Ma, G., Xiao, M., Zhang, Z. & Chan, C. T. Emergence, coalescence, and topological properties of multiple exceptional points and their experimental realization. *Physical Review X* **6**, 021007 (2016).
27. Weiyuan, T. *et al.* Exceptional nexus with a hybrid topological invariant. *Science* **363**, eaar7709 (2020).
28. Król, M. *et al.* Observation of second-order meron polarization textures in optical microcavities. *Optica* **8**, 255–261 (2021).
29. Kavokin, A., Malpuech, G. & Glazov, M. Optical spin Hall effect. *Phys. Rev. Lett.* **95**, 136601 (2005). URL <http://link.aps.org/doi/10.1103/PhysRevLett.95.136601>.

30. Jiahuan, R. *et al.* Nontrivial band geometry in an optically active system. *Nature Communications* **12**, 1 (2021).
31. Zhen, B. *et al.* Spawning rings of exceptional points out of Dirac cones. *Nature* **525**, 354–358 (2015).
32. Zasedatelev, A. V. *et al.* Single-photon nonlinearity at room temperature. *Nature* **597**, 493 (2021).
33. Terças, H., Flayac, H., Solnyshkov, D. D. & Malpuech, G. Non-Abelian gauge fields in photonic cavities and photonic superfluids. *Phys. Rev. Lett.* **112**, 066402 (2014). URL <https://link.aps.org/doi/10.1103/PhysRevLett.112.066402>.

Acknowledgements We acknowledge useful discussions with C. Leblanc. This work was supported by the National Science Centre grants 2019/35/B/ST3/04147, 2019/33/B/ST5/02658 and 2017/27/B/ST3/00271, and the Ministry of National Defense Republic of Poland Program – Research Grant MUT Project 13-995 and MUT University grant (UGB) for the Laboratory of Crystals Physics and Technology for year 2021, and the European Union’s Horizon 2020 program, through a FET Open research and innovation action under the grant agreements No. 899141 (PoLLoC) and No. 964770 (TopoLight). We also acknowledge the support of the ANR Labex Ganex (ANR-11-LABX-0014), and of the ANR program "Investissements d’Avenir" through the IDEX-ISITE initiative 16-IDEX-0001 (CAP 20-25). P.G.L. acknowledge the support of the UK’s Engineering and Physical Sciences Research Council (grant EP/M025330/1 on Hybrid Polaritonics), the support of the RFBR project No. 20-52-12026 (jointly with DFG) and No. 20-02-00919.

Competing interests The authors declare no competing interests.

Correspondence Correspondence related to the experiments should be addressed to Jacek.Szczytko@fuw.edu.pl (JS); Barbara.Pietka@fuw.edu.pl (BP); Correspondence related to theory should be addressed to dmitry.solnyshkov@uca.fr (DS); guillaume.malpuech@uca.fr (GM).

Data availability statement

The datasets generated during and/or analysed during the current study are available in the Open Science Framework (OSF) repository,

https://osf.io/jnx8k/?view_only=16426f9a35404264badaaa93162060a7

Supplementary Information

In this Supplementary Information, we provide more details on the behavior of the Hermitian part of the Hamiltonian of our system. We demonstrate how the Hamiltonian parameters are extracted from the experiment, including the non-Hermiticity (linear dichroism). Finally, we demonstrate that the winding of the real effective field constrains the possibility of a non-Hermitian topological transition with annihilation of the exceptional points: The annihilation is only possible if the total winding of the real effective field is zero.

Topology of the Hermitian Hamiltonian: Theory In this section, we illustrate the topological transitions concerning the Hermitian part of the two-band Hamiltonian (1) of the main text describing the intersection of cavity modes with different numbers. This Hamiltonian is shown below for

convenience, together with the definitions:

$$H_{\mathbf{k}}^{real} = \begin{pmatrix} \frac{E_H^{N+2} + E_V^N}{2} + \frac{\hbar^2 k_x^2}{2m_x} + \frac{\hbar^2 k_y^2}{2m_y} & \Delta - \beta' k^2 - \beta(k_x - ik_y)^2 \\ \Delta - \beta' k^2 - \beta(k_x + ik_y)^2 & \frac{E_H^{N+2} + E_V^N}{2} + \frac{\hbar^2 k_x^2}{2m_x} + \frac{\hbar^2 k_y^2}{2m_y} \end{pmatrix}, \quad (S1)$$

where E_H^{N+2} and $m_H \sim N + 2$ are the energy and mass, of the $N + 2$ th H-polarised mode and E_V^N and $m_V \sim N$, are the energy and mass of the V-polarised mode number N . k_x, k_y are the 2D wave vector components. The spin-independent masses m_x and m_y are determined by the birefringence (n_e, n_o) and the angle of the optical axis θ , according to the following expressions ⁷:

$$\frac{1}{m_x} = \frac{1}{2m'_0} \left(\frac{n_o^2 \sin^2 \theta + n_e^2 \cos^2 \theta + n_e^2}{n_e^2 n_o^2} \right), \quad (S2)$$

$$\frac{1}{m_y} = \frac{1}{2m'_0} \left(\frac{n_e^2 + n_o^2}{n_e^2 n_o^2} \right), \quad (S3)$$

where m'_0 is the mass at the central frequency (between the two modes in question). β is the magnitude of the TE-TM spin orbit coupling. $\beta' = \frac{\hbar^2(m_V - m_H)}{2m_H m_V}$ and $\Delta = (E_H^{N+2} - E_V^N)/2$. This Hermitian Hamiltonian can be written as a linear combination of identity and Pauli matrices which defines a real effective magnetic field Ω_r acting on the polarization pseudo-spin. The two non-zero components of the field are $\Omega_r^x = \Delta - \beta' k^2 - \beta(k_x^2 - k_y^2)$ and $\Omega_r^y = -2\beta k_x k_y$.

The pseudospin of a given eigenstate is either aligned or anti-aligned with the effective field (so far as the Hamiltonian remains Hermitian). Experimentally, this pseudospin corresponds to the Stokes vector of light, calculated using the following expressions:

$$\begin{aligned} S^1 &= \frac{I_V - I_H}{I_H + I_V}, \\ S^2 &= \frac{I_D - I_A}{I_D + I_A}, \\ S^3 &= \frac{I_R - I_L}{I_R + I_L}, \end{aligned} \quad (S4)$$

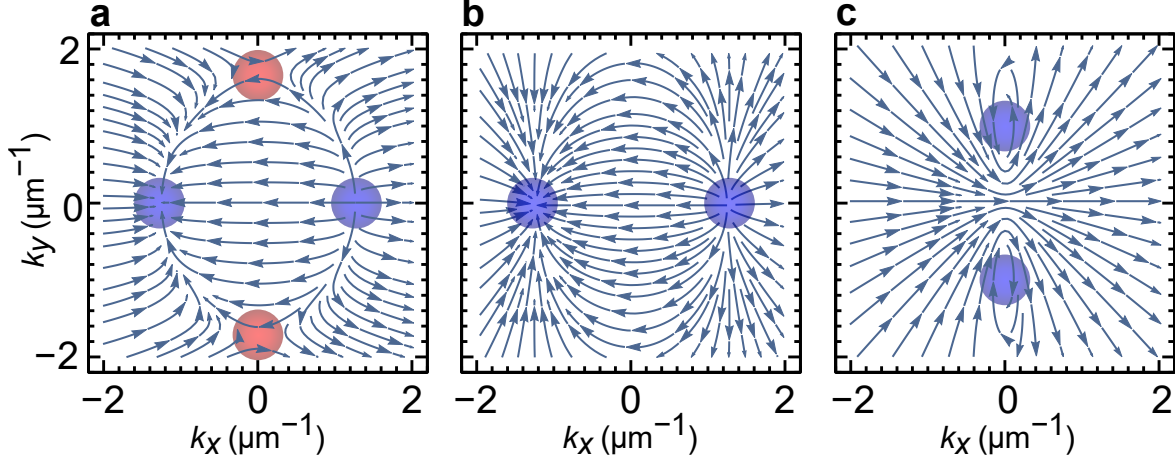


Figure S1: **Pseudospin textures for the Hermitian Hamiltonian:** **a** trivial case $\beta < \beta'$, **b,c** topologically non-trivial case $\beta > \beta'$ with positive and negative detunings. The red marks shows the Dirac points of winding number +1 and the blue marks the Dirac points of winding number -1

where the I_s are the intensities in each of the polarizations, which can be measured experimentally or calculated theoretically as the absolute value squared of the eigenstate wavefunction in the corresponding basis. Each pseudospin component is an average value of the corresponding spin operator represented by a Pauli matrix.

The case $\beta' = 0$ has already been considered in ^{8,33}. The two parabolas are split at $k = 0$, with different possible signs of this splitting (band detuning).

For positive detuning, the TE-TM splitting compensates this splitting along k_x leading to a linear crossing. On the contrary, the TE-TM splitting is changing sign along k_y and adds to the $k = 0$ splitting. As a result, along k_y the two parabola get away the one with respect to the other and do not cross. The resulting spectrum shows two tilted Dirac cones at $\pm k_{0x}$. The winding number

of the effective field around these two points is the same (+1), as shown in Fig. S1b showing the distribution of the pseudospin (and effective field) texture in the reciprocal space. This winding is inherited from the winding number 2 of the TE and TM modes. The Berry topological charge is $+1/2$. This topological phase remains while β' increases up to $\beta' = \beta$ where two new crossing points between the parabola appear at k_{0y} which sets at infinity when the transition occurs. These crossing points correspond to tilted Dirac cones. The winding number of the in-plane pseudo-spin around these two points is (-1) and the Berry topological charge (-1/2), as shown on Figure S1-b. The sum of the topological charges of the 4 Dirac points is zero and the bands are overall topologically trivial which allows the non-Hermitian topological transition we explore in the main text.

For negative detuning (Fig. S1c), the winding of the two Dirac points does not change, but their positions in reciprocal space are rotated by $\pi/2$ and the particular field distribution changes from monopolar to Rashba.

Topology of the Hermitian Hamiltonian: Experiment Cavities filled with birefringent nematic liquid crystal allows for realization of both topologically-distinct cases mentioned above: with non-trivial total winding 2 and trivial total winding 0 (discussed in the main text), depending on voltage applied to the cell. For large enough energy detuning between the two modes of interest, the relative non-Hermiticity is weak enough so that the measured pseudo-spin is simply aligned with the real effective magnetic field (Hermitian limit). In such a case, the winding of the real field in reciprocal space can be determined experimentally through polarization resolved tomography.

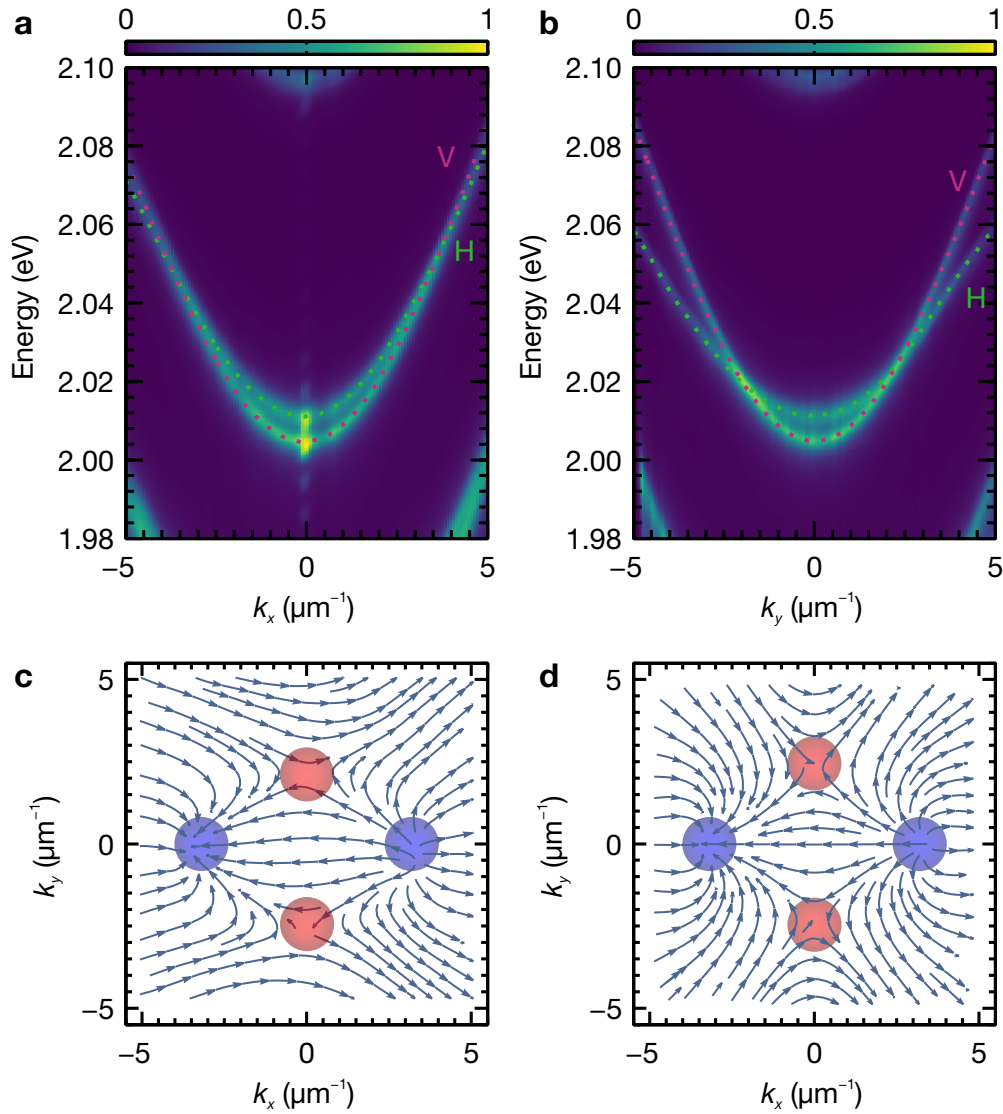


Figure S2: **4 diabolical points case**. Experimental dispersion relation along **a** k_x and **b** k_y directions observed at 1.39 V applied to the microcavity, corresponding to the case with total winding 0. Energy of the bands visible in horizontal (vertical) polarization is marked by green (purple) dashed line. **c** Experimental and **d** simulated by Berreman method pseudospin texture in S_1 - S_2 plane of lower energy band.

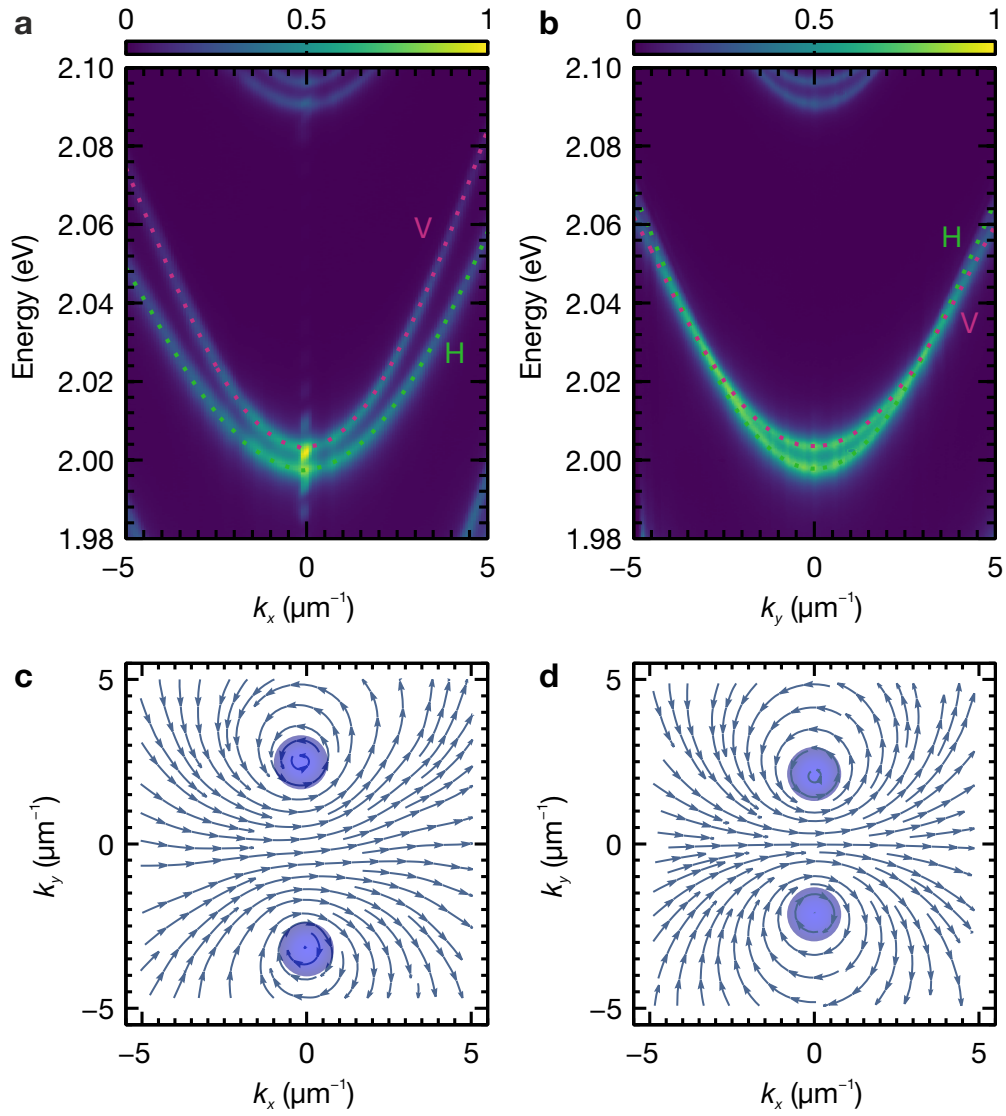


Figure S3: **2 diabolical points case**. Experimental dispersion relation along **a** k_x and **b** k_y directions, observed at 11 V applied to the microcavity, corresponding to the case with winding 2. Energy of the bands visible in horizontal (vertical) polarization is marked by green (purple) dashed line. **c** Experimental and **d** simulated by Berreman method pseudospin texture in S_1-S_2 plane of lower energy band.

Experiments described in this section were performed on a sample analogous to the one described in the main text, but with wider LC layer of around $3.9 \mu\text{m}$.

Fig. S2 presents realization of the case with winding 0, discussed in detail in the main text. Fig. S2a,b presents experimental dispersion relation along k_x and k_y directions observed with 1.39 V applied to ITO electrodes. At this voltage, the numbers of the modes differ by 2, and both modes cross each other along both wave vector directions. Experimentally determined pseudospin texture in S_1 – S_2 plane of the lower energy band is plotted in Fig. S2c. It matches the Berreman matrix model presented in Fig. S2d, showing 0 total winding.

With amplitude of external voltage of 11 V modes with the same mode numbers are close to degenerate, as shown on experimental dispersion relations in Fig. S3. In this case modes crosses each other only along k_y direction. Resulting pseudospin texture in S_1 – S_2 plane shows two 2D monopoles with total winding number of 2 in both experiment Fig. S3c and Berreman model simulations Fig. S3d.

The Dirac points appear along the Y axis because of the negative value of the detuning in the experiment, but their winding is that of the TE-TM field, as expected.

Hamiltonian parameters The parameters of the Hermitian Hamiltonian (1) are extracted from the fit of the dispersion in the two perpendicular directions. The fits are shown in Fig. S4. In a given direction, the average of the two parabolicity coefficients (inverse masses) of the two polarizations, provides the value of $1/m_x$ and $1/m_y$. Then, the difference between the two parabolicities in the

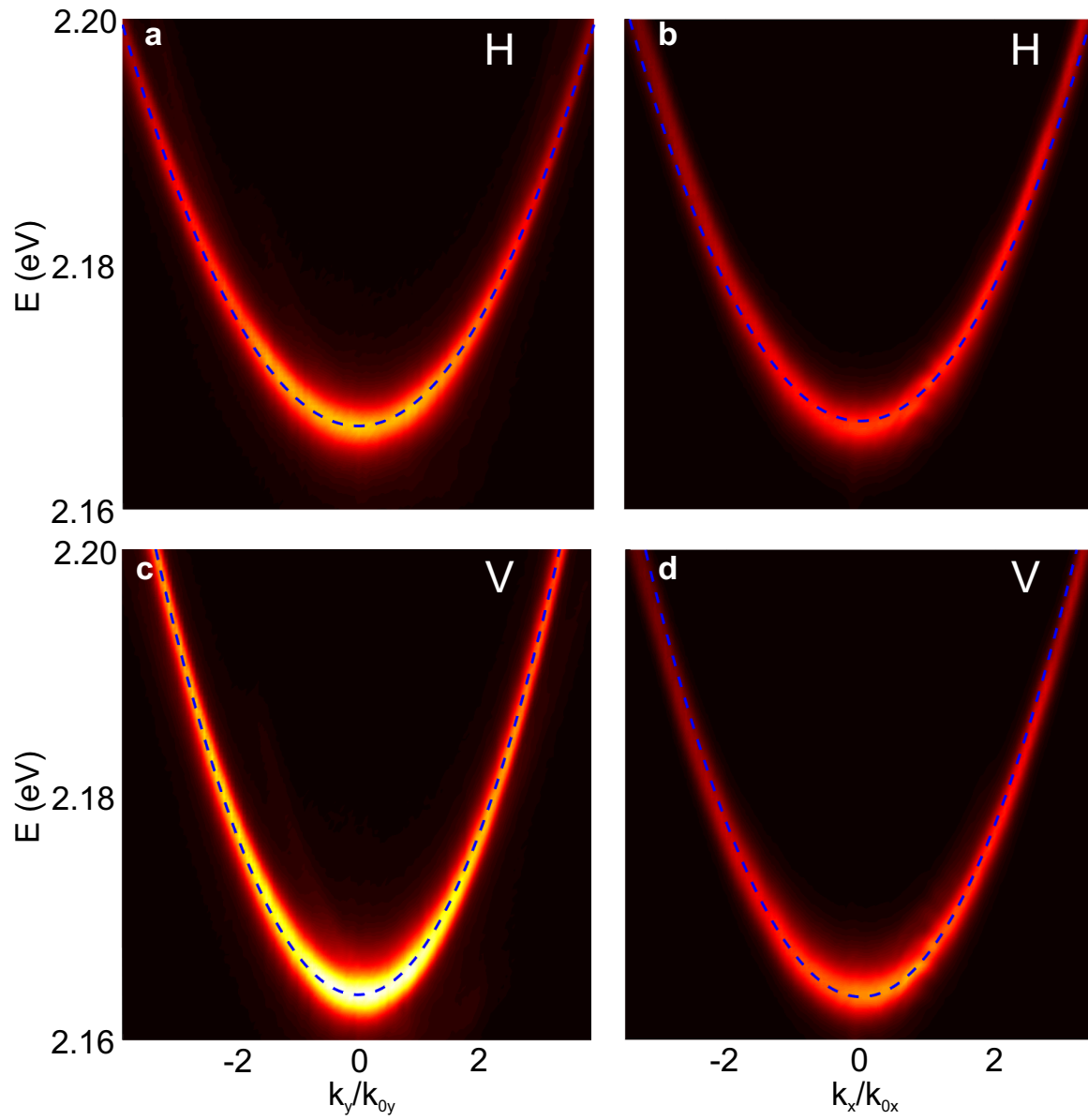


Figure S4: **Fit of the dispersions.** Fit of the polarization-resolved dispersions in the two perpendicular directions. The false color map shows the reflectance as a function of wave vector and energy. Fitting allows to obtain the spin-independent masses m_x and m_y , as well as the polarization splittings β and β' .

two polarizations is $\beta + \beta'$ for Y direction and $\beta - \beta'$ for X direction. Fitting both allows to extract β and β' separately.

Non-Hermitian parameter In Fig. S5, we show an example of a spectrum of reflectance in two polarizations, clearly demonstrating different linewidths. The experimental points for each of the two polarizations are fitted with the Voigt function, as explained in Methods. We stress that while the non-Hermiticity of the Hamiltonian is a single constant, the linewidth at each particular wave vector is determined by the imaginary part of the corresponding eigenstate. Only at the positions of the Dirac points of the Hermitian Hamiltonian does the linewidth of the eigenstates correspond directly to the non-Hermiticity of the Hamiltonian $\delta\Gamma$. It is also the maximal possible imaginary part of the energy that could be observed for any wave vector. This is what we use to extract the non-Hermitian parameter $\delta\Gamma$.

Hermitian winding and annihilation of exceptional points We consider a two-band system described by a Hamiltonian depending on a two-dimensional wave vector. The Hermitian part of the Hamiltonian is characterized by a presence of diabolical (Dirac) points. The two-band nature allows writing the Hamiltonian as a superposition of Pauli matrices. For many typical situations, such Hamiltonians can be written using only two Pauli matrices that we can choose to be σ_x and σ_y (massless Dirac Hamiltonian, Rashba and Dresselhaus spin-orbit couplings, TE-TM spin-orbit coupling for photons), whereas the third Pauli matrix σ_z , responsible for a symmetry breaking, opens the gap at the diabolical points (the mass term in the Dirac Hamiltonian or the Zeeman splitting for electrons and photonic modes). In this case, it is possible to characterize each of the

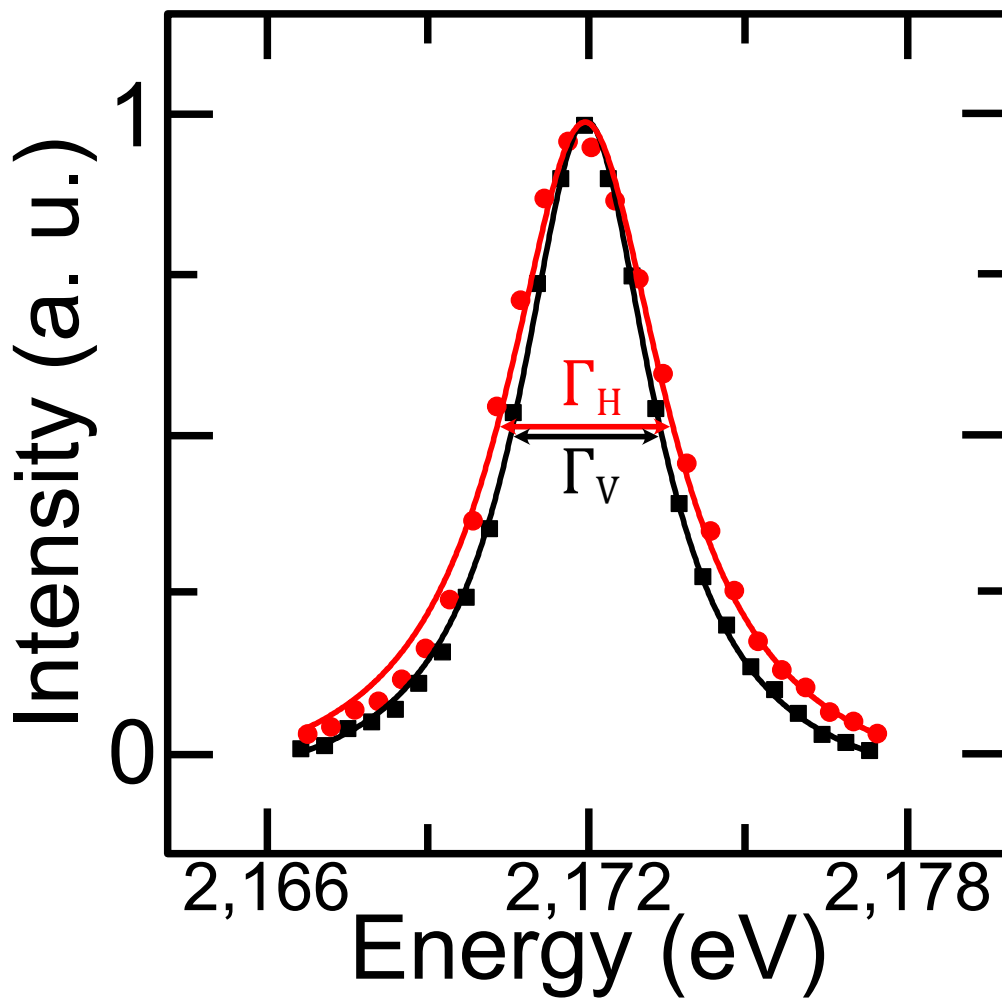


Figure S5: **Polarization-resolved reflectance spectrum.** The reflectance in polarizations H and V, measured at the position of the diabolical point and plotted as a function of energy. The difference of linewidths is approximately 13%.

diabolical points and the whole reciprocal space by winding numbers, which, in turn, determine the topology (the Chern number) of the bands once the gap is opened.

We then consider the evolution of the Hamiltonian with an addition of non-Hermiticity, described by a single constant parameter (independent of the wave vector). Without loss of generality, we consider the non-Hermitian contribution to be described by the Pauli matrix σ_x . In presence of the non-Hermiticity, each of the diabolical points gives rise to two exceptional points.

Thanks to the use of the Pauli matrices, it is possible to map the system's Hamiltonian to a spin-1/2 in a magnetic field, using the so-called pseudospin formalism, where the terms of the Hamiltonian are considered as an effective field. In the presence of a non-Hermiticity, this effective field has both real and imaginary components, $\Omega = \Omega' + i\Omega''$. An exceptional point requires the real and imaginary parts of the effective field to be equal to each other in magnitude and perpendicular in direction: $\Omega' = \Omega''$ and $\Omega' \perp \Omega''$.

Since in our case the direction of the imaginary field is fixed $\Omega'' = \Omega'' e_x$, and the real field is in the XY plane, the exceptional points can only be found where the x-component of the real field is zero $\Omega' = \Omega' e_y \Leftrightarrow \Omega'_x = 0$. This condition constrains their evolution in the reciprocal space when the imaginary field is increased $\Omega'' \rightarrow \infty$ (or the real field is decreased $\Omega' \rightarrow 0$). The location of the ensemble of the points $\Omega'_x = 0$ is determined by the winding of the real field at the diabolical points. With the increase of Ω'' , the exceptional points are moving towards infinity. **If no points, where the condition for the real part $\Omega'_x = 0$ is satisfied, can be found at infinity, then the exceptional points must annihilate for some finite critical value Ω''_c .** Two cases are

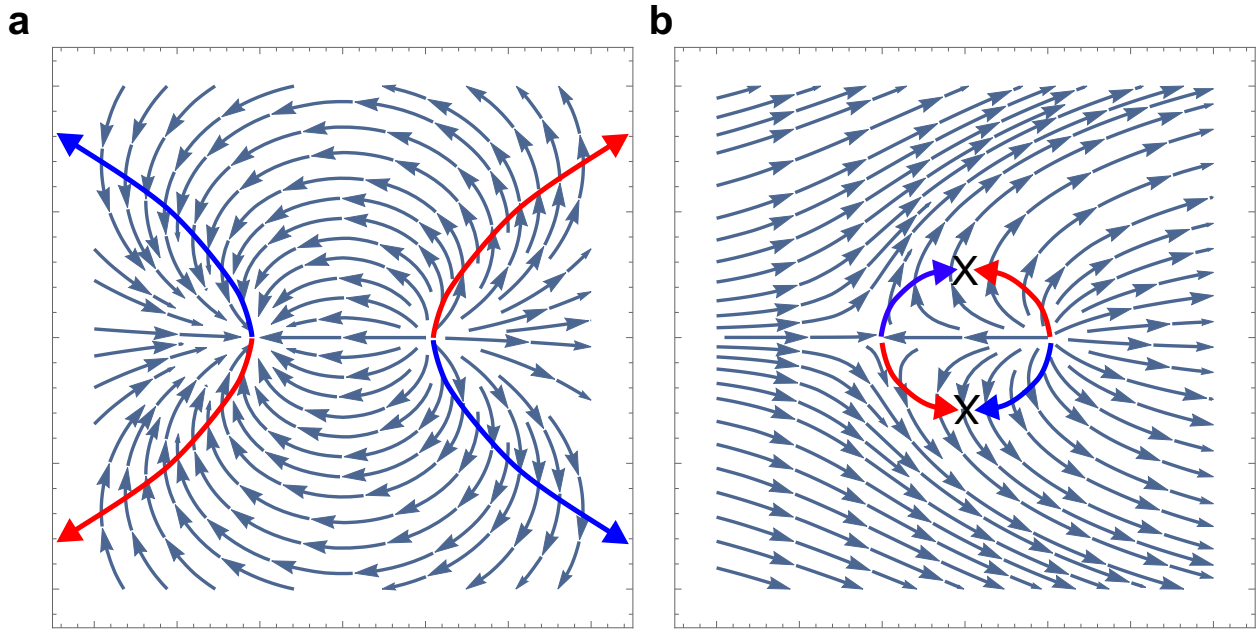


Figure S6: **Hermitian winding and annihilation of exceptional points.** (a) Non-zero total winding of the real field, the exceptional points do not annihilate. (b) Zero total winding of the real field, annihilation of exceptional points. The trajectories of the exceptional points are shown with red and blue arrows (corresponding to the winding of the exceptional points themselves). Crosses mark the annihilation points.

possible:

1. The overall winding of the real field is a non-zero integer. In this case, the orientation angle θ_r of the real field at infinity changes at least once between $\theta_r = 0$ and $\theta_r = 2\pi$, necessarily going through $\pi/2$ and $3\pi/2$, where $\Omega'_x = 0$. Therefore, the exceptional points can be found for any value of Ω'' up to infinity, and thus they cannot annihilate (or if they annihilate accidentally, they must then reappear when Ω'' is increased).
2. The overall winding of the real field is zero. In this case, the orientation angle of the real field θ_r at infinity is constrained to an interval which may not include $\pi/2$ or $3\pi/2$. In this case, the exceptional points cannot be present at infinity, and therefore they must annihilate for a finite value of Ω''_c .

The two situations are illustrated in Fig. S6. Panel (a) shows the case with total winding 2 with a dipolar texture typical for the TE-TM field. The trajectories of the exceptional points are shown with red and blue lines, which are defined by the condition $\Omega'_x = 0$ (vertical orientation of the real field). At a large scale, the relative position of the two diabolical points does not play any role and the texture is given by $\theta_r = 2\varphi$ (where φ is the polar angle of the wave vector). The exceptional points at infinity are therefore necessarily located at $\varphi = \pm\pi/4, \pm3\pi/4$ (while initially they move from the diabolical points in the vertical direction).

The second situation is illustrated by Fig. S6(b), where the overall winding of the real field is zero. The angle of the real field at infinity is $\theta_r = 0$ and there can be no exceptional points. The

condition $\Omega'_x = 0$ (vertical real field) gives the trajectories of the exceptional points shown in the figure, with the annihilation points marked with crosses.

Finally, the winding of the exceptional points themselves is shown with a color of the arrows (red and blue).

The winding of an exceptional point is the winding of the phase of the complex eigenenergies. Indeed, the energy of a second-order exceptional point is given by

$$E = \pm \sqrt{\alpha q} e^{iw\phi/2} \quad (\text{S5})$$

where $w = \pm 1$ is precisely the winding number and q is the absolute value of the parameter controlling the deviation from the exceptional point, for example, the wave vector (measured from the exceptional point). This eigenenergy can be obtained as a solution for different Hamiltonians, with different variation of real and imaginary effective fields. Below, we show that when the imaginary effective field Ω'' is constant, the winding of the exceptional point can be easily determined from the texture of the real effective field Ω' . The most general form of a Hamiltonian of such type is

$$\begin{aligned} \hat{H} &= \alpha q (\sigma_x \cos \varphi + iw \sigma_y \sin \varphi) \\ &+ a ((\sigma_x \cos \theta + \sigma_y \sin \theta) \\ &+ ia (\sigma_x \cos(\theta \pm \pi/2) + \sigma_y \sin(\theta \pm \pi/2))) \end{aligned} \quad (\text{S6})$$

where the a gives the values of the real and imaginary effective field oriented at an angle θ and $\theta + \pi/2$ respectively, equal and perpendicular at the exceptional point, w is the winding of the parameter-dependent part of the real effective field and α is its strength. The eigenenergies of this

Hamiltonian are given by

$$E \approx \pm \sqrt{q} \sqrt{2\alpha a} e^{\pm i w \varphi / 2} e^{-i \theta / 2} \quad (\text{S7})$$

We see that the winding of an exceptional point is determined by the winding w of the original diabolical point, modified by the relative angle of the real and imaginary fields at each exceptional point $\pm \pi / 2$.